# Transitional response of double-mode Faraday waves in a brimful container

Shimin Zhang and Zhiliang Lin*

*State Key Laboratory of Ocean Engineering,*
*Shanghai Jiao Tong University, Shanghai 200240, People's Republic of China*
*and Marine Numerical Experiment Center, School of Ocean and Civil Engineering,*
*Shanghai Jiao Tong University, Shanghai 200240, People's Republic of China*

(Received 25 July 2024; accepted 11 March 2025; published 31 March 2025)

This paper experimentally investigates the transitional response of double-mode Faraday waves in a brimful circular container subjected to vertical vibration with parameters near the overlap of two instability tongues. Special attention is paid to the temporal evolution of primary wave components from the initial rest state to the final resonant state. To characterize the nonlinear pattern-forming dynamics, local amplitude variations are measured using a laser Doppler vibrometer, and spatial changes in surface patterns are reconstructed through a modified free-surface synthetic Schlieren method. With rapid ramping of the forcing acceleration, we find that mode transition occurs in a double-mode system where one mode with a lower natural frequency prevails in the transient pattern competition. Phenomenological analysis of single-mode experiments identifies the linear growth rate $\alpha \propto \epsilon$, where $\epsilon$ is the dimensionless forcing distance, and shows nonlinear coefficients $\beta_5 > 0 > \beta_8$, indicating supercritical and subcritical excitation for the fivefold and eightfold modes, respectively. Incorporating mode suppression and fifth-order terms, coupled amplitude equations can be completed to describe the observed transitional responses of double-mode Faraday waves. This work provides insights into the complex pattern-forming dynamics of Faraday waves in multimode systems.

DOI: 10.1103/PhysRevFluids.10.034003

## I. INTRODUCTION

Faraday waves are commonly excited in a periodically vibrating liquid system when the forcing amplitude surpasses a critical magnitude, called the Faraday threshold. Faraday [1] investigated experimentally the dynamical response of a vibrating liquid layer by measuring light reflection and discovered that the surface interface oscillated at half the driving frequency. Subsequently, synchronous Faraday waves were observed experimentally, leading to a challenging contradiction to Faraday's earlier findings [2]. To address this conundrum, linear stability analysis was proposed to explain the primary dynamics of an inviscid liquid system undergoing vertical vibration via solutions of an undamped Mathieu equation [3]. The resulting tongue-like boundaries implied the possible presence of subharmonic resonance and/or harmonic resonance, depending on the driving parameters, and showed the validity of the findings of Faraday [1] and Matthiessen [2]. In a later study, Floquet theory was used to analyze the instability of the viscous Navier-Stokes equations and predict theoretically the effect of fluid viscosity on wavelength selection and stability threshold [4]. The results showed excellent agreement with experimental measurements [5,6]. According to linear stability analysis, harmonic solutions also exist [7] under certain conditions, such as in thin fluid layers and at low driving frequencies; these were subsequently confirmed experimentally

*Contact author: linzhiliang@sjtu.edu.cn

 

[8]. Later, many experimental and theoretical studies were conducted on nonlinear pattern-forming dynamics near a bicritical point, also called a codimension 2 point, where subharmonic-harmonic mode competition and transition arose [9–11].

Experimental investigations into pattern competition between two or more subharmonic modes have also been widely conducted for various container geometries [12–15]. To address the formation of competing patterns in Faraday-wave experiments, a phenomenological model was introduced [14], which shed light on the dynamical mechanism of low-dimensional chaos. Reduced amplitude equations for the primary wave components in the double-mode system of Ciliberto and Gollub [12] were derived using center-manifold and normal-form theories [16,17]. Subsequently, normal-form equations were reduced to a one-dimensional (1D) amplitude equation for single-mode dynamics and a system of two coupled amplitude equations for double-mode interactions [18]. An averaged Lagrangian method was also employed to analyze the slowly varying amplitudes of two nearly degenerate subharmonic modes, identifying period-doubling bifurcations that could influence the symmetry of the system [19].

Mode transition with hysteresis was observed when slowly ramping the forcing parameters across the boundary separating two regions corresponding to different modes [9,13]. In the double-mode system studied by Ciliberto and Gollub [12], a remarkable numerical result obtained by Meron and Procaccia [17] was that a pure fourfold mode prevailed when competing sevenfold and fourfold modes were excited simultaneously. Of particular interest is whether an additional mode can be excited during this formation process. Although the transitional response was observed numerically by Meron and Procaccia [17], it has not yet been observed experimentally, which may emerge in experiments involving rapid changes in driving parameters, with the free surface initially at rest.

In Faraday-wave experiments, various factors inducing system dissipation significantly influence pattern formation, including the bulk viscosity [20–23], the surface rigidity [24], and the meniscus near the lateral boundary [25–27]. Specifically, the existing meniscus geometry emits harmonic traveling waves (also called meniscus waves or edge waves), which always mix with Faraday waves and can be effectively suppressed by filling the liquid to the brim [28,29]. In this paper, a vibrated liquid layer in a brimful container of small aspect ratio and circular geometry is employed to experimentally investigate the transitional behavior of double-mode Faraday waves. In addition, the sidewall plays a significant part in pattern formation in small containers, where Faraday waves are typically expressed in the finite form of modal decomposition [3,29,30]. Hence, nonlinear pattern formation and mode transition in the experiments can be understood in terms of a set of coupled amplitude equations for the primary modes.

However, experimental measurement of slowly varying mode amplitudes in multimode systems poses challenges. Optical images are usually Fourier transformed to obtain the time-dependent amplitudes of the excited modes [12,13]; however, this is arduous and time consuming. A much more effective method uses two photodiodes with known locations to acquire two-phase mode amplitudes in real time for a double-mode system [31]. Inspired by Simonelli and Gollub [31], slow variations in mode amplitudes are investigated herein using single-point surface evaluation with a laser Doppler vibrometer (LDV) at two points selected according to the spatial dependence of the two standing modes. Single-point surface detection relies on the absence of slow rotation in a double-mode competition. This has been previously reported [32] and is also observed in our experiments. In practice, these limitations have little influence on the analysis of transitional pattern formation, especially during the early stages. Another reason for implementing the free-surface synthetic Schlieren (FS-SS) method [33] is that it provides full spatial three-dimensional (3D) reconstructions of surface disturbances, enabling us to quantify the response process of the surface pattern as it transits from a rest state to a final state. Recently, the FS-SS method has been extensively employed for surface measurement of pure cross-waves [34], surface topography induced by a bouncing droplet [35], three-wave resonant interactions [36], and electrostatically forced Faraday waves [37]. In the present work, a modified FS-SS method [30] is applied for surface reconstruction in a circular domain.

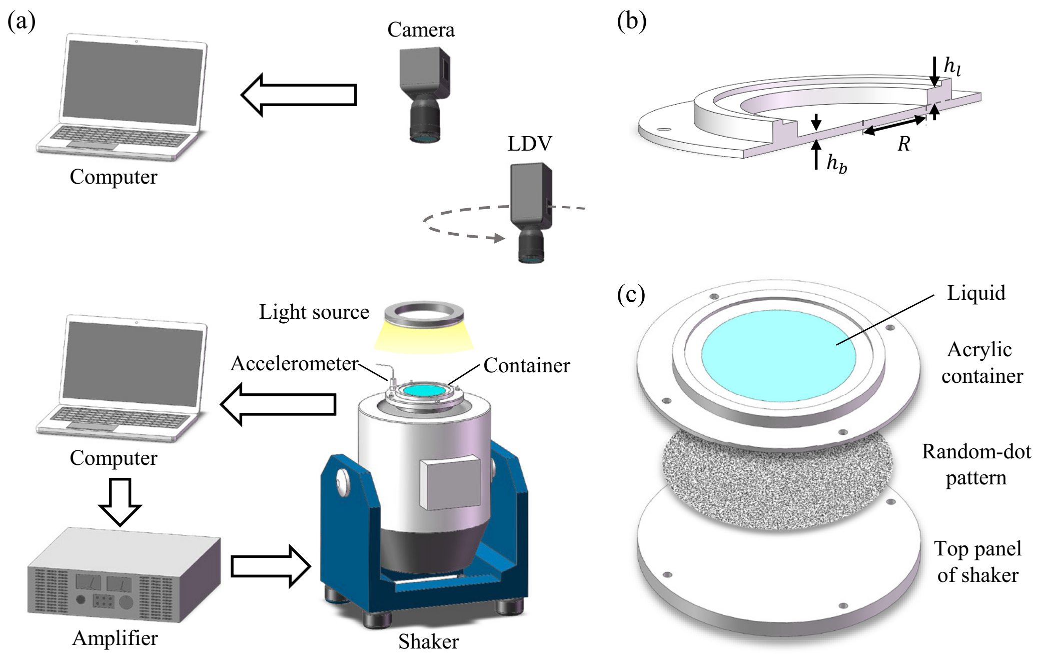


FIG. 1. Experimental setup and cylindrical container. (a) The electromagnetic shaker, amplifier, accelerometer, and computer with built-in function generator constitute a closed-loop control system, which provides consistent vertical vibration of the container. Instantaneous surface patterns are captured by a visualization system using a ring-shaped LED light source and a high-speed camera. Local surface elevation data are recorded by LDV. (b) The geometry of the cylindrical container is illustrated in the transverse profile. The inner cylindrical space is to be filled with liquid. The outer circular prevents any potential spillage. (c) A random-dot pattern, necessary for surface reconstruction, is inserted between the shaker and the acrylic container when filled to the brim with liquid.

The paper is organized as follows. Section II introduces the experimental setup, procedures, and two methodologies for surface evaluation. Section III displays the parameter-space diagram of the double-mode system of interest. Section IV A defines the corresponding mode amplitudes in two coupled amplitude equations. Section IV B analyzes the slow growth of the primary component in single-mode responses, approximated by a form of one-dimensional amplitude equation, and identifies the relationship between the corresponding coefficients and the forcing parameters. Section IV C reports the transitional response in the double-mode system, which is related to mode suppression.

## II. EXPERIMENTAL METHODOLOGY AND FREE SURFACE EVALUATION

### A. Experimental setup

Figure 1(a) shows the experimental setup. Faraday waves are excited in a vertically vibrating container with an effective acceleration of $(1 - \Gamma_0 \cos 2\pi f t)g$, where $\Gamma_0$ is dimensionless acceleration amplitude, $f$ is driving frequency, and $g$ is gravitational acceleration. With two forcing parameters $\Gamma_0$ and $f$ prescribed, steady sinusoidal vibration of the liquid system is guaranteed by a closed-loop control system consisting of an electromechanical shaker (ESS-050, China), an acceleration generator (Amber, China), a power amplifier (PA-1200, China), and an accelerometer. A high-speed camera (SpeedCam MacroVis EoSens, Germany) with lens (Tokina atx-i 100 mm F2.8 FF MACRO, Japan) and ring-shaped LED light source are positioned vertically above the container to record the instantaneous pattern evolution. The distance $h_c$ between the camera and the liquid surface is approximately 1.3 m. The light source, equipped with a diffuser, provides strong and uniform light irradiation of the liquid interface. This facilitates the capture of distinct images of the otherwise distorted random-dot pattern, required for high-resolution surface reconstruction, as detailed in Sec. II D. Due to limitations in camera storage, intermittent imaging at a high frame rate is employed to capture the primary pattern evolution of Faraday waves. Meanwhile, a single-point laser Doppler vibrometer (LV-S01, China) is employed to measure the long-duration oscillation of a single point on the surface of the waves. The working LDV apparatus unavoidably obstructs the camera's view, and so we perform two distinct trials separately utilizing the camera and LDV under identical driving conditions. The LDV is mounted on a swivel platform and repositioned out of the camera's view when the camera is working. Figure 1(b) illustrates the geometric arrangement of the cylindrical container, which is precisely manufactured from a single piece of acrylic plate. The container has a cylindrical inner domain of depth $h_l = 6$ mm and radius $R = 45$ mm, and a transparent base of thickness $h_b = 3$ mm. An outer circular structure is designed to prevent spillage during vibration experiments. As shown in Fig. 1(c), the container with a random-dot background beneath is mounted on the top panel of the shaker.

### B. Experimental procedure

Distilled water is selected as the test liquid. To ensure a pinned contact line and suppress the appearance of meniscus waves (also known as edge waves), the cylinder is fully filled to its brim with the test liquid, as suggested by Shao *et al.* [29]. Due to exposure to an open-air environment, slow evaporation of water and slight surface pollution are unavoidable. We implement two procedures to mitigate any potential impact on surface characteristics including static contact angle and surface tension. First, we repeatedly check the surface condition at the boundary and add liquid to the brim if necessary after each vibration test. Second, we clean the container and change the liquid every 90 minutes or if a polluted surface is observed, following the approach described by Henderson and Miles [38]. These preparations help guarantee the experiments are reproducible. The liquid properties, although not measured, are assumed to be those of pure water at temperature ($25 \pm 0.5\,^{\circ}$C), with liquid density $\rho = 997$ kg/m$^3$, surface tension $\sigma = 72$ mN/m, and dynamic viscosity $\mu = 10^{-3}$ Pa s.

As described in Sec. II A, two surface evaluation methods are utilized. Initially, vibration experiments are conducted with fixed forcing parameters, and single-point measurements are obtained using an LDV at a sampling rate of 96 000 Hz. This allows us to ascertain the excitation of Faraday waves and the lifespan of wave responses, as stated in Sec. II C. If the liquid system exhibits subharmonic resonance (Faraday waves), we repeat the experiment using the same forcing parameters. During the second experiment, a high-speed camera, operating at a frame rate of 500 frames per second and an exposure time of 1.98 ms, captures instantaneous top-view images covering the overall circular liquid interface for a prolonged time ($\geqslant 4/f$). The camera is triggered at numerous discrete instants to record the whole pattern-forming process. By analyzing the camera output, we identify the wave modes excited by the prescribed force and create a phase diagram of Faraday modes within a certain range of driving parameters, as elaborated in Sec. III.

### C. Single-point surface evaluation

LDV is utilized to investigate Faraday waves. Figure 2(a) depicts the operating principle of LDV. Analyses of the reference laser beam and the scattered light from the oscillating liquid system are used to infer the normal wave velocity $V$ through the Doppler effect and the wave elevation $\eta$ through interferometry. The built-in helium-neon laser source used herein provides a low-powered laser beam with emission wavelength of 632.8 nm. It should be noted that the applicability of LDV is limited to weakly steep surfaces because the presence of large wave steepness leads to abrupt loss of refracted signal and erroneous changes in the velocity output. Hence, the detection

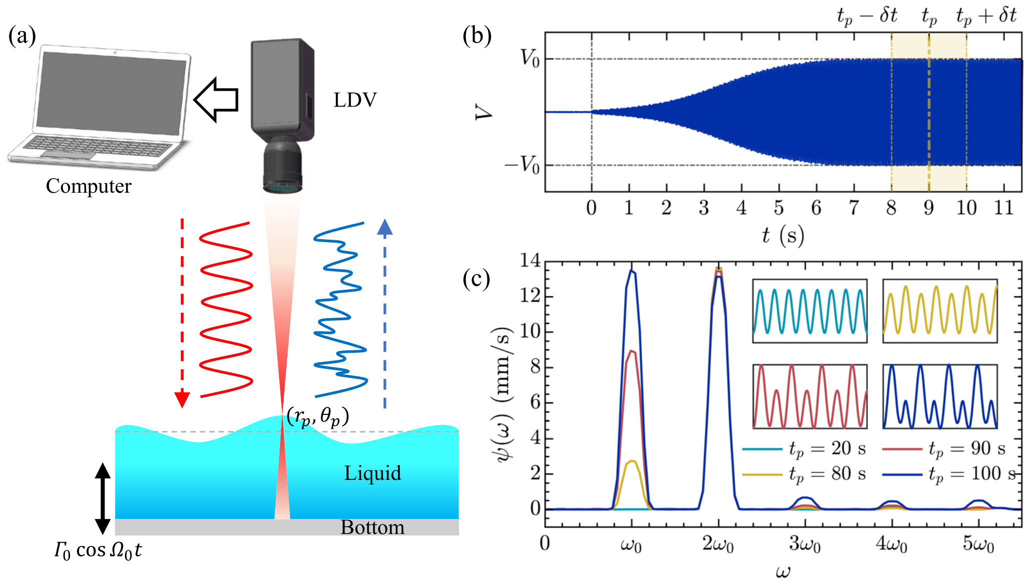


FIG. 2. Methodology and postprocessed outputs for single-point surface evaluation. (a) Time history of surface velocity of a single point $(r_p, \theta_p)$ obtained using LDV. This is achieved by analyzing signals from the reference laser beam (red) and the reflected laser beam (blue). (b) Real-time output signal from LDV at the beginning of vibration evaluated for typical experimental observation for $\Gamma_0 = 0.16$ and $f = 17.45$ Hz. (c) Instantaneous velocity amplitude spectra $\psi(\omega)$ at four instants $t_p$ are obtained by postprocessing the sampling data within $[t_p - \delta t, t_p + \delta t]$ with $\delta t \approx 1$ s. Corresponding velocity signals are shown in the insets. Note that the shaker oscillates at frequency $2\omega_0$.

point $P$ of laser projection, defined by the polar coordinates $(r_p, \theta_p)$ whose origin is at the center of the container, is selected artificially at a slightly weak-slope location. Different points are used according to pattern structures and investigation requirements. To capture a sufficiently strong laser reflection signal, the optical probe of LDV is located at a prescribed low elevation above the liquid surface. Conventionally, surface evaluation by LDV requires the addition of light-scattering particles to the water, such as $TiO_2$ [39] and PS-MMA [24]. For our surface reconstruction applications, we keep the liquid transparent to preserve the interference of light reflected from the bottom of the container.

Figure 2(b) shows a single-point detection output signal obtained using LDV during the initiating periods of an experiment where $\Gamma_0 = 0.16$ and $f = 17.45$ Hz. Operating at constant frequency, the vibration of the shaker takes a short time (several seconds) to reach the desired velocity amplitude $V_0$ such that $V_0 = \Gamma_0 g/2\pi f$. The amplitude of the forcing acceleration is therefore rapidly increased from zero to a prescribed value $\Gamma_0$ as indicated by the positive envelope in Fig. 2(b). The output signal $V$ within a short time window $[t_p - \delta t, t_p + \delta t]$ is processed by a fast Fourier transform (FFT) with a flat-top window function, which reduces spectral energy leakage for multifrequency sinusoidal signal processing, to obtain the instantaneous velocity amplitude spectrum $\psi(\omega)$ at any time $t_p$ and given coordinates $(r_p, \theta_p)$. A value of $\delta t \approx 1$ s is typically selected in practice to capture a sufficiently large number of wave periods. Additionally, Fig. 2(c) displays the time-dependent $\psi(\omega)$ and temporal signals $V(t)$ at four instants. As demonstrated in the insets, the LDV signal remains sinusoidal until Faraday waves emerge. The $\psi(\omega)$ curves indicate that the liquid surface oscillates primarily at multiple angular frequencies of $l\omega_0$ ($l = 1, 2, 3, \dots$). The shaker oscillates at $2\omega_0$, and so it introduces corresponding oscillation and associated harmonics, which mix with resonant wave responses. Although $\psi(l\omega_0)$ ($l \geqslant 2$) is unreliable for determining harmonics in pattern responses, the subharmonic components are clean and exhibit noticeable growth during the response process.

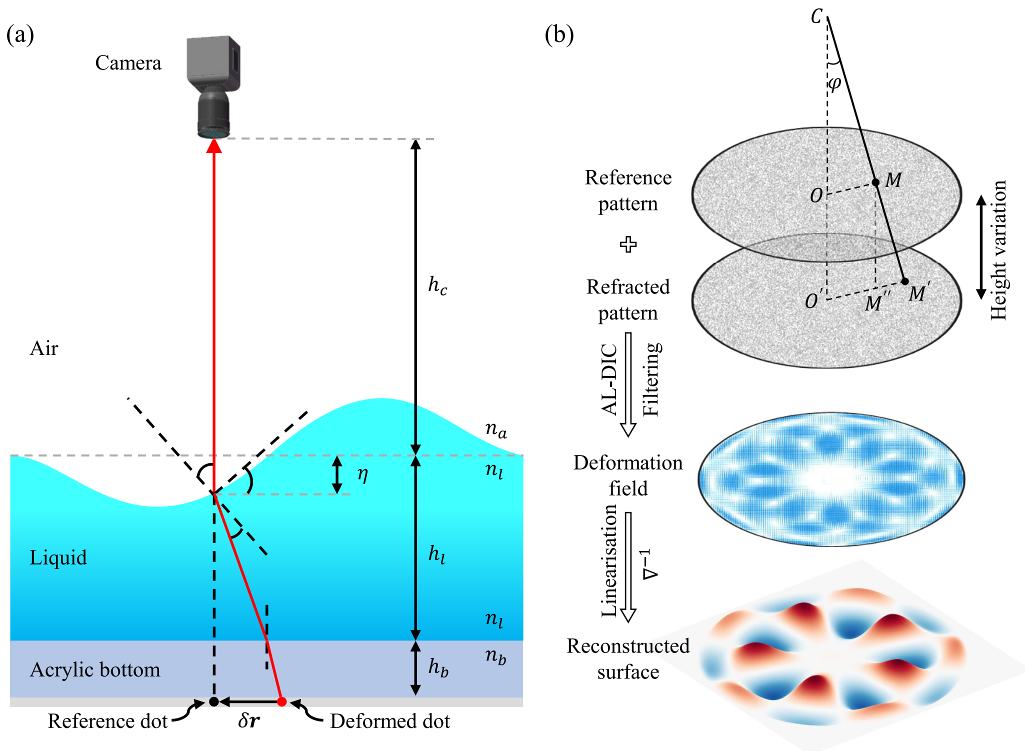


FIG. 3. Schematic of the full 3D spatial surface reconstruction procedure. (a) Optical configuration for the experimental system. Surface slope leads to the refracted pattern, which gives rise to the relation between surface gradient $\nabla\eta$ and deformation field $\delta\boldsymbol{r}$. (b) Two primary steps in surface reconstruction. The height variation between reference and refracted patterns results in the generation of vibration-induced deformation noise $\boldsymbol{M'M''}$. A filtering procedure is performed after the AL-DIC calculation to obtain a smoothed deformation field. The quiver plot specifies the processed deformation field, where deep blue regions manifest larger distortion. Then, a linearization procedure based on Eq. (1) and an inverse gradient operation $\nabla^{-1}$ are employed to accomplish full 3D spatial surface reconstruction.

Therefore, time-varying $\psi(\omega_0)/\omega_0$, denoted by $\Psi$, can be used to characterize the local amplitude evolution of subharmonic responses.

### D. Full 3D spatial surface reconstruction

The FS-SS method [33] is utilized to obtain a full 3D spatial surface reconstruction of Faraday waves, and thus identify the primary wave components of the resonant response. Figure 3(a) depicts the optical configuration for the liquid system. Before vibrations commence, a reference random-dot pattern is captured, and a calibration factor $a_c = 0.103$ mm/pixel and a spatial resolution of 0.822 mm are calculated. Light refraction through the sloped air-liquid interface causes the background pattern to be optically distorted. We consider the linear relation between the surface elevation gradient $\nabla\eta$ and the deformation field $\delta\boldsymbol{r}$ (unit: mm), given by

$$\nabla\eta = -\frac{a_c}{(1 - n_a/n_l)h_p}\delta\boldsymbol{r}, \quad (1)$$

where $n_a$ and $n_l$ denote the optical indices of air and liquid, respectively, and $h_p$ is an effective surface-background height defined as $h_p = h_l + (n_l/n_b)h_b$ with $n_b$ the optical index of the acrylic bottom of the container. Equation (1) requires three approximation conditions to be met. In the experimental setup, $h_c/R \gg 1$ in order to satisfy the paraxial approximation. The present experiments entail generation of weak-amplitude waves with relatively long wavelength $\lambda$, resulting in small $|\eta|/h_l$ that precludes ray-crossing and small $|\eta|/\lambda$ that approximates the averaged wave slope. These satisfy weak amplitude and weak slope approximations.

Figure 3(b) illustrates the surface reconstruction, which is based on the two-step FS-SS method. First, the deformation field $\delta\boldsymbol{r}$ of the refracted pattern is calculated using the augmented Lagrangian digital image correlation algorithm (AL-DIC) [40]. The resulting raw deformation field then undergoes filtering to reveal the real deformation field. Second, the surface gradient $\nabla\eta$ is calculated by means of a linearization procedure [Eq. (1)], and the free surface topography is reconstructed by the inverse operation $\nabla^{-1}$ on $\nabla\eta$. Details of the formula used for $\nabla^{-1}$ have been provided by Zhang *et al.* [30].

Due to the vertical motion of the random pattern, a time-dependent height variation $\Delta h_v$ exists between the reference and the refracted patterns. In Fig. 3(b) light refraction is not taken into account, and points $M$ in the reference pattern and $M'$ in the refracted pattern correspond to the same imaging pixel owing to the same viewing angle $\varphi$. Due to $\Delta h_v$, reference point $M$ undergoes deformation $\delta\boldsymbol{r}_v$ that is equal to $\boldsymbol{M'M''}$, called vibration-induced deformation noise. From geometry, $\delta\boldsymbol{r}_v = -(\Delta h_v/h_c)\cdot\boldsymbol{OM}$, causing the background pattern to zoom in and out during vibration. In practice, however, the camera may not view vertically at the center of the circular liquid interface, giving rise to an overall translation of the pattern, which also contributes to $\delta\boldsymbol{r}_v$. A Cartesian coordinate is therefore utilized at the circular liquid interface, with the origin at its center and the $\hat{\boldsymbol{x}}$ and $\hat{\boldsymbol{y}}$ axes parallel to the perpendicular arrangements of the imaging pixels. With $\boldsymbol{OM} = (x, y)$, the linear form of $\delta\boldsymbol{r}_v$ is given by

$$\delta\boldsymbol{r}_v = (c_x x + d_x)\hat{\boldsymbol{x}} + (c_y y + d_y)\hat{\boldsymbol{y}}. \tag{2}$$

Here $c_x$ and $c_y$ denote zoom coefficients; and $d_x$ and $d_y$ denote translation coefficients. We can simply subtract $\delta\boldsymbol{r}_v$ from the raw deformation field by filtering out its best-fit plane in the form of Eq. (2), as detailed in the example presented by Zhang *et al.* [30].

### III. PHASE DIAGRAM OF DOUBLE-MODE SYSTEM

In the experiments, two forcing parameters, $\Gamma_0$ and $f$, are prescribed to excite Faraday waves from the rest interface. The driving amplitude is increased rapidly from 0 to $\Gamma_0$ as depicted in Fig. 2(b), which corresponds to a swift transition along the $f$ line in Fig. 4. In a brimful circular cylinder, a Faraday mode with a single symmetry can be identified by the pair $(\nu, \zeta)$ with the non-negative integer $\nu$ and the positive integer $\zeta$ characterizing the azimuthal number and the radial nodal number, respectively. In the present work, we specifically examine the response behavior in a double-mode system where two nearly degenerate modes, (5, 2) and (8, 1), are simultaneously resonant.

Figure 4(a) shows the phase diagram for the double-mode system in the vicinity of the bicritical point where $\Gamma_0 \leqslant 0.2$ and 17.4 Hz $\leqslant f \leqslant$ 17.6 Hz. Based on the pattern formation behavior, we identify two single-mode responses, (8, 1) and (5, 2), which exhibit purely eightfold and fivefold surface patterns, respectively. Additionally, we classify two double-mode responses, $C_{5,8}$ and $(8, 1)^*$. Their distinction lies in the final states where both the eightfold mode and fivefold mode compete with each other in the $C_{5,8}$ phase while the eightfold mode completely prevails over the fivefold mode in the $(8, 1)^*$ phase. In brief, $C_{5,8}$ is competing while $(8, 1)^*$ is prevailing. In $(8, 1)^*$, mode transition from a transient fivefold mode [see Fig. 4(b)] to a final eightfold mode [see Fig. 4(d)] is particularly interesting, and so serves as the primary focus of this study.

In Fig. 4(a) two solid curves, $\Gamma_\nu$ ($\nu = 5, 8$), indicate the Faraday thresholds of the two $\nu$-fold modes. In addition, the boundary $\Gamma_C$ separates the single-mode response regime of (5, 2) from the competing response regime of $C_{5,8}$, and the boundary $\Gamma_S$ separates the prevailing response regime of $(8, 1)^*$ from the competing response regime of $C_{5,8}$. All these boundaries converge at a bicritical point, $(f_B, \Gamma_B)$, also known as a codimension 2 point. When subjected to a higher driving

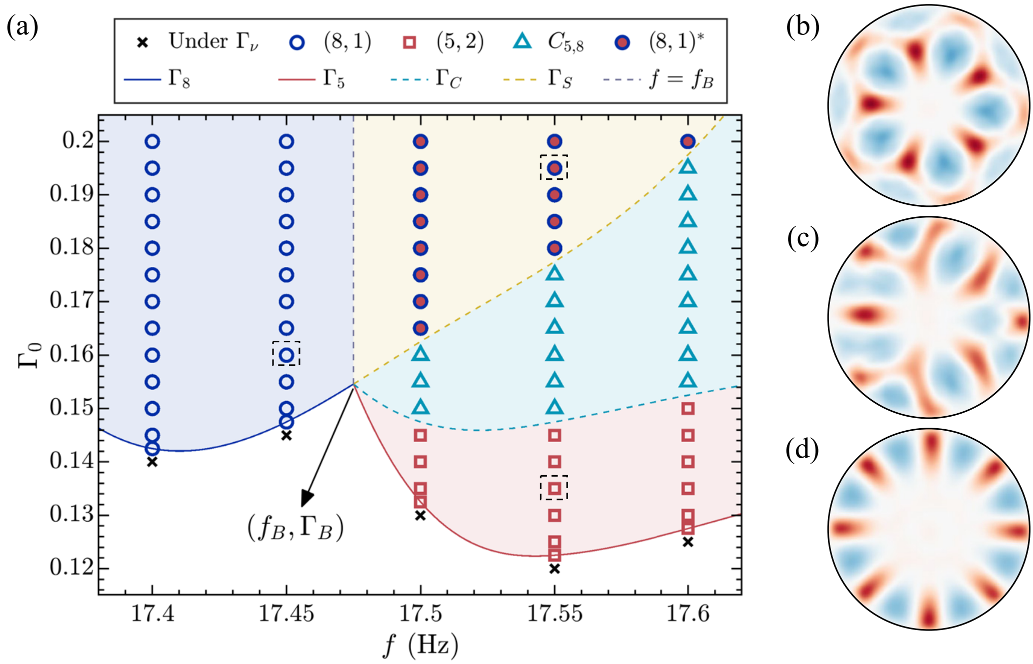


FIG. 4. Phase diagram of the double-mode system of interest as a function of the forcing parameters, $\Gamma_0$ and $f$. (a) Observed wave responses can be classified into single-mode responses, (8, 1) and (5, 2), double-mode prevailing responses $(8, 1)^*$, and double-mode competing responses $C_{5,8}$. Different response regions are separated by five boundaries ($\Gamma_8$, $\Gamma_5$, $\Gamma_C$, $\Gamma_S$, and $f = f_B$), which all intersect at the labeled point $(f_B, \Gamma_B)$. Dashed squares around three points indicate parameter pairs that will be studied in Sec. IV. (b) A pure fivefold pattern and (c) a competitive pattern, both transient, and (d) a pure eightfold pattern, obtained in $(8, 1)^*$ with $\Gamma_0 = 0.195$ and $f = 17.55$ Hz, are presented in (b), (c), and (d), with red regions indicating $\eta > 0$, and blue regions indicating $\eta < 0$.

acceleration than the Faraday threshold $\Gamma_\nu$, a $\nu$-fold mode can be detected by LDV and the camera. The onset is commonly determined by slowly ramping the driving parameters until a certain mode is triggered or breaks down [13,15,29]. An essential criterion for threshold identification is based on the requirement that the subharmonic response observed near the onset occurs after a relatively lengthy period of vibration [41]. In our experiments, we identify $\Gamma_\nu$ using the minimal forcing acceleration required to trigger the $(\nu, \zeta)$ mode after a sufficiently long time (4 minutes according to our experimental experience). Note that the measured $\Gamma_\nu$ is slightly overestimated. Moreover, the accelerations, $\Gamma_C$ and $\Gamma_S$, required to excite $C_{5,8}$ and $(8, 1)^*$, are estimated by averaging the corresponding lower and higher accelerations. In summary, the double-mode parameter-space diagram of interest resembles that presented in the work by Ciliberto and Gollub [13], where only the lower-frequency mode prevails in the overlapping regions. However, an extra region of $f > f_B$ concerning the double-mode prevailing response $(8, 1)^*$ is distinguished from the intersection of two tongues, while only the single-mode response (8, 1) is available for $f < f_B$, indicating extreme suppression of the right-hand mode. The natural frequency $f_\nu$ of the $\nu$-fold mode is identified as the frequency at the bottom of the corresponding tongues so that $f_5 > f_B > f_8$.

## IV. RESULTS AND DISCUSSION

### A. Spatial distribution and amplitude equation

For the $(\nu, \zeta)$ mode, the surface displacement $\eta(r, \theta, t)$ takes the form of [30]

$$\eta(r, \theta, t) = \sum_{m=1}^{M} \sum_{n=1}^{N} a_{m,n}(t) \cos m\nu\theta \, \mathrm{J}_{m\nu}(\delta_{m\nu,n} r), \tag{3}$$

where $\delta_{m\nu,n}$ is the $n$th zero of the $m\nu$-order Bessel function $J_{m\nu}$. Equation (3) indicates that the $\nu$-fold mode is a superposition of the $\nu$-basis modes $(m, n)_\nu$ with the corresponding spatial dependence $\cos m\nu\theta \, \mathrm{J}_{m\nu}(\delta_{m\nu,n} r)$. The primary mode ($m = 1$) is $(1, \zeta)_\nu$ oscillating at $\omega_0$ and these $m \geqslant 2$ modes are the harmonics oscillating at $m\omega_0$. In the double-mode system of interest, each primary wave component $(1, \zeta)_\nu$ has a spatiotemporal expression

$$A_\nu(t) \cos \omega_0 t \cos \nu\theta \, \mathrm{J}_\nu(\delta_{\nu,\zeta} r),$$

where $A_\nu(t)$ is the primary mode amplitude evolving on a timescale much longer than $1/\omega_0$. Therefore, the dynamical state of the double-mode system is specified by the slowly varying coefficients $A_\nu(t)$ ($\nu = 5, 8$). Inspired by the fundamental work of Meron and Procaccia [16–18], we have two coupled amplitude equations, $A_\nu(t)$ ($\nu = 5, 8$), in the form of

$$\begin{aligned} \frac{\mathrm{d}A_5}{\mathrm{d}t} &= \alpha_5 A_5 - \beta_5 A_5^3 - g_{5,8} A_8^2 A_5 + \text{h.o.t.} \\ \frac{\mathrm{d}A_8}{\mathrm{d}t} &= \alpha_8 A_8 - \beta_8 A_8^3 - g_{8,5} A_5^2 A_8 + \text{h.o.t.}, \end{aligned} \tag{4}$$

where $\alpha_\nu$ represents the linear growth rate of the $\nu$-fold mode, and $\beta_\nu$ and $g_{\nu,\nu'}$ ($\nu' \neq \nu$) denote coefficients linked to a cubic term and a coupling term, respectively. Additionally, the abbreviation h.o.t. stands for higher-order terms. Although derived at the bicritical point, Eqs. (4) are instrumental in elucidating various aspects of double-mode pattern formation in the vicinity of the bicritical point. According to the observed mode suppression, $g_{5,8} > 0 > g_{8,5}$, which aligns with the derivation of Meron [18].

In the experiments, we measure the local amplitude $\Psi = \psi(\omega_0)/\omega_0$ of the wave components to characterize the slow evolution of two primary modes. Specifically, the spatial difference in the surface distribution of the $(8, 1)$ and $(5, 2)$ modes is used to differentiate between their amplitudes in a transient competing pattern as displayed in Fig. 4(c). Owing to the small contribution of the eightfold component to the surface disturbance within the region of $r \leqslant 0.5$ [see Fig. 4(d)], we can measure $\Psi_5$ at a point $P_5$ ($r_p \approx 0.4R$) to approximate the slow evolution of the $(5, 2)$ mode. As shown in Fig. 4(b), although both fivefold and eightfold modes contribute to $\Psi_8$, obtained at a relatively near-boundary point $P_8$ ($r_p \approx 0.9R$), we can deduce the evolution of the eightfold mode from comparison with $\Psi_5$. With the known spatial dependence at a detection point $(r_p, \theta_p)$, the relationship between $A_\nu$ and $\Psi_\nu$ is given by $A_\nu = \chi_\nu \Psi_\nu$, where $\chi_\nu = \cos \nu\theta_p \, \mathrm{J}_\nu(\delta_{\nu,\zeta} r_p)$; this can also be identified from $\chi_\nu = A_\nu^s/\Psi_\nu^s$ in which the superscript "$s$" indicates saturation data.

Figure 5(a) shows the measured local amplitude $\Psi_5$ for the fivefold mode excited in the experiment for $f = 17.55$ Hz and $\Gamma_0 = 0.135$; and $\Psi_8$ for the eightfold mode is measured with $f = 17.45$ Hz and $\Gamma_0 = 0.16$. The saturated local amplitude $\Psi_\nu^s$ can be easily obtained, as displayed in Fig. 5(a). With $M = 6$ and $N = 15$, we utilize Eq. (3) to fit the surface reconstructions at the final steady state and obtain the fitting coefficient $a_{m,n}(t)$ to evaluate the oscillation of the corresponding wave components $(m, n)_\nu$. Figures 5(b) and 5(c) display the calculations of $|a_{m,n}|_{\max}$ ($m = 1, 2$), the maximal absolute values of $a_{m,n}(t)$ during a wave period $2/f$, for $\nu = 5$ and 8, respectively. The primary mode $(a, \zeta)_\nu$ and the harmonic mode ($m = 2$) are identified from these peak modes as labeled in Figs. 5(b) and 5(c). From $a_{1,\zeta}(t) = A_\nu^s \cos \omega_0 t$, we obtain the primary mode amplitudes $A_5^s = 1.4601$ mm and $A_8^s = 1.9732$ mm, as shown in Figs. 5(d) and 5(e). Therefore, the coefficients $\chi_\nu = A_\nu^s/\Psi_\nu^s$ are calculated, giving $\chi_5 = 8.4032$ and $\chi_8 = 7.9194$. Due to the linear relationship,

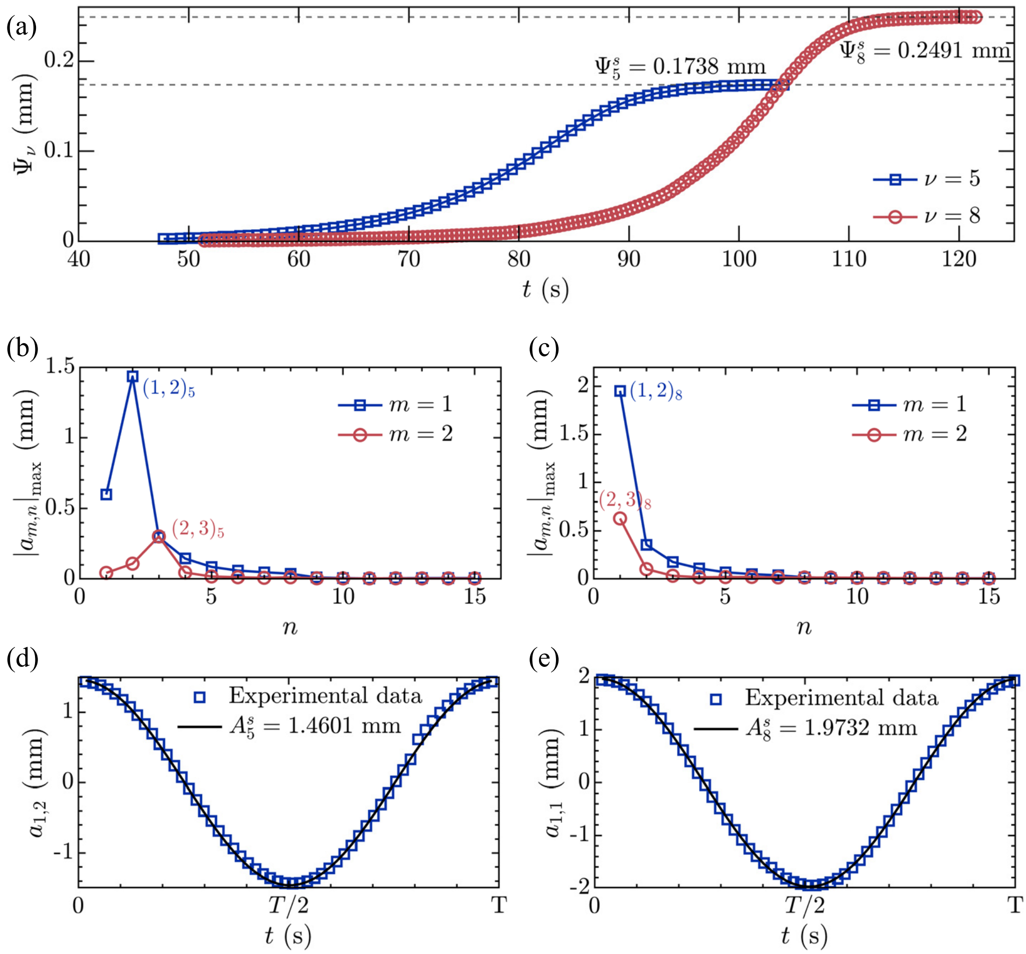


FIG. 5. Spatiotemporal characteristics of the single-mode responses (5, 2) and (8, 1). (a) The local amplitude $\Psi_\nu(t)$ obtained by LDV at the point $P_\nu$ ($\nu = 5, 8$) is employed to characterize the single-mode pattern formation. The saturation $\Psi_\nu^s$ is obtained when resonance reaches steady state. From the fitting results of $|a_{m,n}|_{\max}$, the indicated peak modes are identified as the primary mode ($m = 1$) and the harmonic mode ($m = 2$) for (b) (5, 2) and (c) (8, 1). (c) Saturated mode amplitude $A_\nu^s$ determined from the best fit of $a_{1,\zeta} = A_\nu^s \cos \omega_0 t$ for (d) (5, 2) and (e) (8, 1).

we can quickly obtain the primary mode amplitude $A_\nu$ based on the LDV measurements $\Psi_\nu$, not from the fits of the full spatial surface reconstructions.

### B. Estimates from single-mode responses

The process of single-mode pattern formation is well understood, as depicted in Fig. 5(a). When the forcing acceleration surpasses the Faraday threshold, the primary mode is initiated at the air-liquid interface and becomes noticeable over time. After prolonged oscillations, the primary wave component and its harmonics gradually reach saturation, achieving energy equilibrium in the vibrating system. To explain the measured evolution of $A_\nu$, we introduce the following amplitude equation. In the single-mode regimes of Fig. 4, (5, 2) and (8, 1) are not excited simultaneously, so

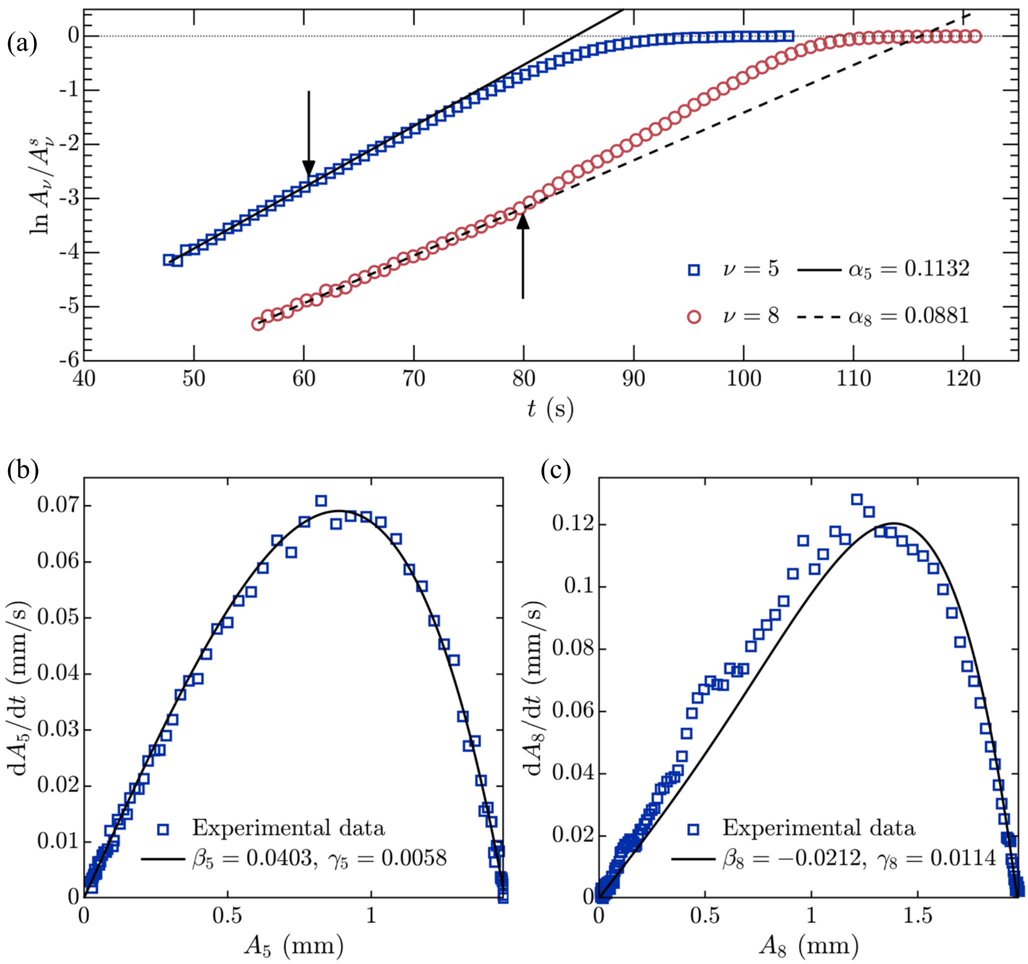


FIG. 6. Estimates of linear growth rates $\alpha_\nu$ of the $\nu$-fold mode. (a) Best linear fits of $\ln(A_\nu/A_\nu^s)$ ($\nu = 5, 8$) during the initial response periods (prior to the time marked by black arrows) indicate $\alpha_5 = 0.1132$ at $\epsilon_5 = 0.1020$ and $\alpha_8 = 0.0881$ at $\epsilon_8 = 0.0847$. With the known $\alpha_\nu$ in (a), the fitting results based on Eq. (5) for (b) fivefold and (c) eightfold pattern formation are illustrated with the indicated coefficients $\beta_\nu$ and $\gamma_\nu$. The values of $\beta_8 < 0$ imply the subcriticality of the (8, 1) mode.

the coupling terms in Eqs. (4) can be eliminated, giving

$$\frac{\mathrm{d}A_\nu}{\mathrm{d}t} = \alpha_\nu A_\nu - \beta_\nu A_\nu^3 - \gamma_\nu A_\nu^5, \tag{5}$$

where the fifth-order term $-\gamma_\nu A_\nu^5$ is necessary for potential subcriticality when $\beta_\nu < 0$. Additionally, from Eq. (5), the steady-state condition $\mathrm{d}A_\nu/\mathrm{d}t = 0$ yields that the corresponding solution $A_\nu^s$ exhibits subcritical or supercritical bifurcation for $\beta_\nu < 0$ or $\beta_\nu > 0$, respectively [18].

Figure 6(a) shows the logarithmic value $\ln(A_\nu/A_\nu^s)$ ($\nu = 5, 8$) versus $t$ for the (5, 2) mode and the (8, 1) mode, as displayed in Fig. 5(a). The initial linear growth of $\ln(A_\nu/A_\nu^s)$ indicates the exponential growth of the mode amplitude $A_\nu$ at early response stage. Two linear fits are used to estimate the linear growth rate $\alpha_\nu$ ($\nu = 5, 8$) of the $\nu$-fold mode, yielding slopes of $\alpha_5 = 0.1151$ and $\alpha_8 = 0.0848$. After certain time periods, marked by the arrows in Fig. 6(a), $A_\nu$ departs from exponential growth due to the nonlinear terms in Eq. (5). An initial downward departure from linear

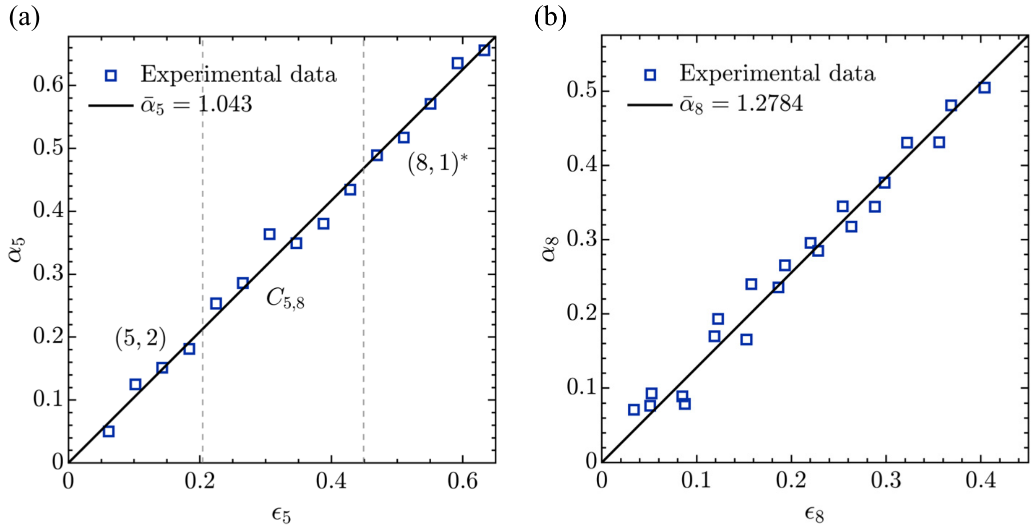


FIG. 7. The linear relationship $\alpha_\nu = \bar{\alpha}_\nu \epsilon_\nu$ implies $\bar{\alpha}_5 = 1.043$ and $\bar{\alpha}_8 = 1.2784$. The two dashed lines in (b) are located at $\epsilon_5 = (\Gamma_C - \Gamma_5)/\Gamma_5$ and $\epsilon_5 = (\Gamma_8 - \Gamma_5)/\Gamma_5$ to separate the three indicated response types.

growth implies a supercritical bifurcation, and an initial upward departure implies a subcritical bifurcation [42]. Specifically, $\ln(A_\nu/A_\nu^s)$ departs downward for $(5, 2)$ and upward for $(8, 1)$, indicating that $\beta_5 > 0$ and $\beta_8 < 0$. Then we utilize Eq. (5) to fit the experimental data $\tilde{\Psi}$, with $\alpha_\nu$ estimated from Fig. 6(a) and $\mathrm{d}A_\nu/\mathrm{d}t$ calculated using centered differences. As depicted in Figs. 6(b) and 6(c), Eq. (5) can approximately explain the $(5, 2)$ and $(8, 1)$ pattern formation. The coefficients derived in Figs. 6(b) and 6(c) demonstrate that $\beta_5 = 0.0403 > 0$ and $\beta_8 = -0.0212 < 0$, which agrees with the derivation by Meron [18] where the sign of $\beta_\nu$ correlates with $f_\nu - f_B$. Therefore, the transition from the rest state to the steady state of the fivefold mode ($\beta_5 > 0$) is continuous via a supercritical bifurcation, whereas the subcritical transition of the eightfold mode ($\beta_8 < 0$) is discontinuous.

By using a similar linear-fitting procedure on $\ln(A_\nu/A_\nu^s)$ for different forcing parameters, one can readily derive the linear growth rate $\alpha_\nu$, even for double-mode responses where the initial response can be considered as a single mode. Given that the fivefold mode consistently precedes the eightfold mode, applying linear fits to $\ln(A_5/A_5^s)$ for $C_{5,8}$ or $(8, 1)^*$ enables the linear growth rate $\alpha_5$ to be determined. Figures 7(a) and 7(b) illustrate the linear relationships between the calculated $\alpha_\nu$ and the reduced parameter $\epsilon_\nu = (\Gamma_0 - \Gamma_\nu)/\Gamma_\nu$. The specific form of $\alpha_\nu$ can be explored as $\alpha_\nu = \bar{\alpha}_\nu \epsilon_\nu$ with $\bar{\alpha}_5 = 1.043$ and $\bar{\alpha}_8 = 1.2784$ identified from the slopes of the two linear fits.

### C. Mode transition in the double-mode system

A forcing acceleration $\Gamma_0 \in (\Gamma_C, \Gamma_S)$ yields $\epsilon_5 > 0 > \epsilon_8$ so that only the fivefold mode is excited initially. Sufficiently large $A_5$ leads to a positive value of $\epsilon_8 \bar{\alpha} - g_{8,5} A_5^2$ in Eqs. (4) that triggers the presence of the eightfold mode, resulting in slow-periodic or chaotic pattern competition. This phenomenon has been widely studied experimentally [12,13] and theoretically [16,17]. When $\Gamma_0$ exceeds $\Gamma_S$, one gets $\epsilon_5 > \epsilon_8 > 0$ so that the fivefold mode occurs more quickly and is more noticeable than the eightfold mode in the experiments. Due to $g_{5,8} > 0 > g_{8,5}$ in Eqs. (4), the eightfold mode eventually prevails over the fivefold mode. Note that suppression of the fivefold mode is strong because the steady amplitude $A_8^s(\epsilon_8)$ transits through a subcritical bifurcation. Herein we focus on the slow evolution of $(8, 1)^*$ excited at $\Gamma_0 = 0.195$ to analyze the mode transition from a rest state to a prevailing state, in accordance with the numerical calculations by Meron and Procaccia [17]. Figure 8(a) shows the curves of $\Psi_5$ and $\Psi_8$, measured at two selected points $P_5$ and $P_8$ via LDV, which characterize the nonlinear dynamics of $(5, 2)$ and $(8, 1)$, respectively. To

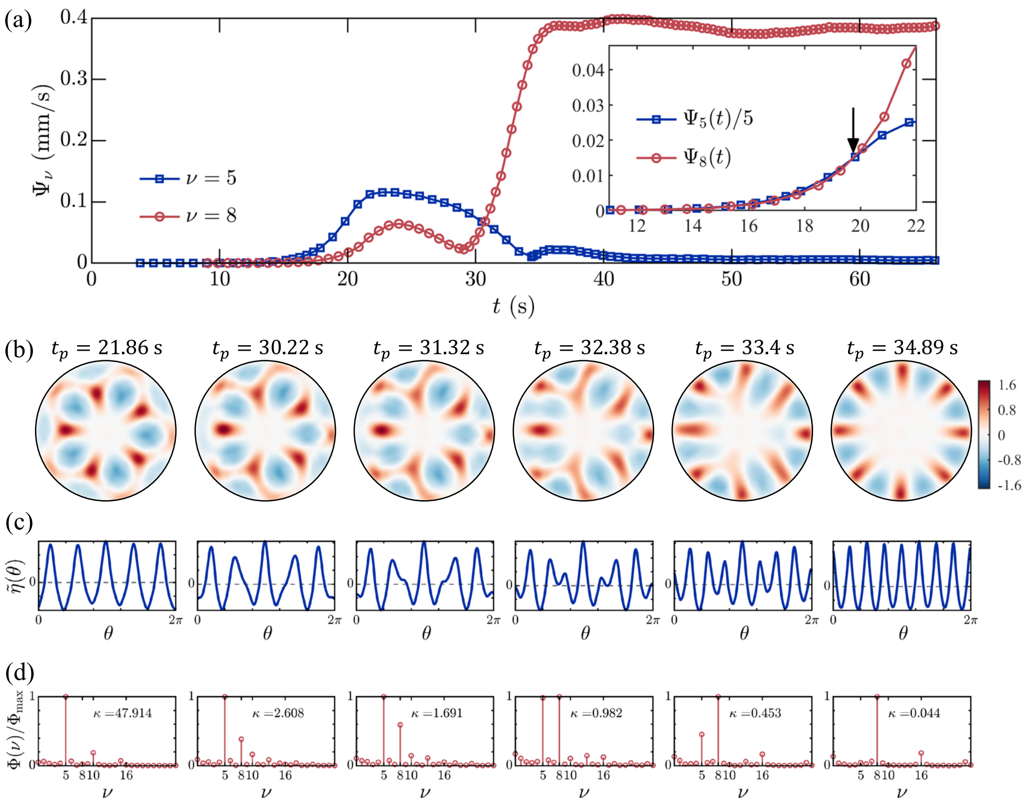


FIG. 8. Spatiotemporal characteristics of the double-mode response $(8, 1)^*$ excited in the experiment for $\Gamma_0 = 0.195$ and $f = 17.55$ Hz. (a) The time-varying $\Psi_\nu(t)$ is obtained at two detection points $P_\nu$ ($\nu = 5, 8$). Inset: The overlap of $\Psi_8(t)$ and $1/5\Psi_5(t)$ indicates the initial appearance of the fivefold component, and so their separation can be utilized to identify the instant at which the eightfold mode can be observed, as indicated by the arrow. (b) Typical patterns for six oscillation cycles ($[t_p - 1/f, t_p + 1/f]$) display the transitional pattern changes of $(8, 1)^*$. The color bar is given for the surface elevation $\eta$ in millimeters. (c) Corresponding azimuthal structures $\tilde{\eta}(\theta)$ are calculated by integrating the radial surface elevation. (d) Corresponding angular power spectra $\Phi(\nu)$ for given $\nu$ are obtained by FFT processing of $\tilde{\eta}(\theta)$, with the factors $\kappa$ [$= \Phi(5)/\Phi(8)$] indicated. The overall slow evolution of the surface patterns in the present experiment is displayed in the supplemental movie [43].

intuitively depict the slow-transition process within 20 s $\leqslant t \leqslant$ 35 s, Fig. 8(b) displays patterns with the largest peak elevation at the six periods of interest $[t_p - 1/f, t_p + 1/f]$. The first pattern is fivefold, the middle four patterns are competing, and the last one is eightfold.

Shortly after the shaker starts, a subharmonic component of the fivefold mode can be observed in Figs. 8(a) and 8(b). Despite the different detection locations, $\Psi_5$ and $\Psi_8$ exhibit consistent growth, as evident in the initial overlap of $\Psi_5/5$ and $\Psi_8$ in the inset of Fig. 8(a). The zoom factor of 1/5 is dictated by the spatial structures of the fivefold mode. Gradually, two curves, $\Psi_5/5$ and $\Psi_8$, start to diverge at the instant marked by the arrow due to the increasing contribution of the eightfold component to $\Psi_8$. The eightfold mode intensifies, initiating intricate structural dynamics through pattern competition. Rapid growth of the eightfold mode suppresses the fivefold mode, which disappears completely after several slow oscillation periods, as depicted in Fig. 8(b).

Following Ciliberto and Gollub [13], we conduct an angular FFT analysis of the six patterns to find all wave components during this transitional response. Figure 8(c) shows the slow transition

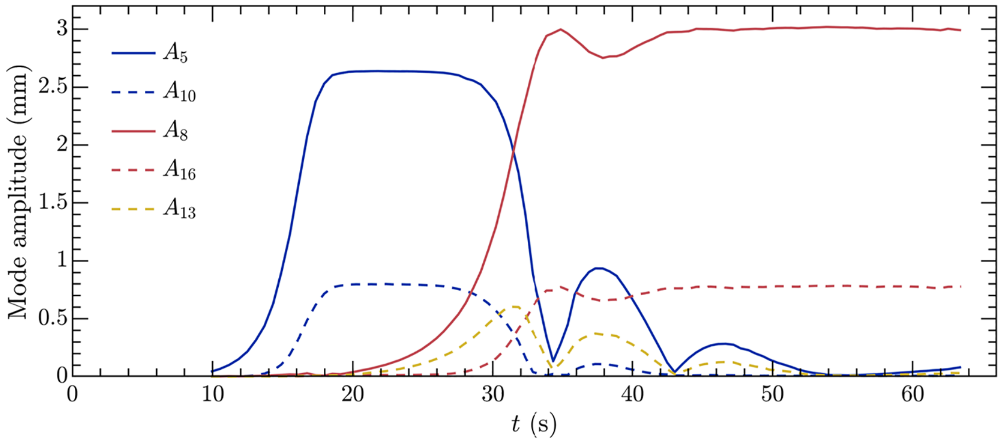


FIG. 9. Slow evolution of mode amplitudes $A_5$, $A_8$, $A_{10}$, $A_{16}$, and $A_{13}$

in the azimuthal structures $\tilde{\eta}(\theta) = \int_0^R \eta(r, \theta)\mathrm{d}r$. FFT analysis of $\tilde{\eta}(\theta)$ yields the angular power spectrum $\Phi(\nu)$ at various $\nu$, and the normalized angular power spectra $\Phi(\nu)/\Phi_{\max}$, where $\Phi_{\max}$ is the maximum of $\Phi(\nu)$, as displayed in Fig. 8(d). The magnitude of $\Phi(5)/\Phi(8)$, denoted as $\kappa$, is calculated for each pattern and is approximately proportional to the mode amplitude ratio of two wave components $(5, 2)$ and $(8, 1)$. An apparent decline in $\kappa$ indicates that $(5, 2)$ vanishes and $(8, 1)$ wins in the pattern competition. Furthermore, discernible peaks at $\nu = 10, 15$ and $\nu = 16, 24$ correspond to the harmonics $(m = 2, 3)$, and those at $\nu = 13, 18, 21$ correspond to the nonlinear modes stemming from the interaction among the two primary modes. Most of these high-order components have relatively small $\Phi(\nu)$, thus barely influencing the evolution of the primary modes. However, their existence may lead to slight rotation of the pattern as displayed in the supplemental movie [43], which is detrimental to single-point detection by LDV. Therefore, it is more accurate to identify mode amplitudes directly from surface reconstructions than by using transformations from $\Psi_5$ and $\Psi_8$. We seek the surface expression for the competing patterns as

$$\eta(r, \theta, t) = \sum_{m=1}^{M} \sum_{n=1}^{N} \sum_{\nu=5,8,13} a_{m,n,\nu}(t) \cos m\nu\theta \, \mathrm{J}_{m\nu}(\delta_{m\nu,n} r), \tag{6}$$

where the mode $\nu = 13$ is incorporated due to its non-negligible amplitude during pattern competition as shown in Fig. 8(d). Similarly, $M = 6$ and $N = 15$ are set in Eq. (6) to fit surface reconstructions. We focus on two primary modes, $(1, 2)_5$ and $(1, 1)_8$, two harmonics, $(2, 3)_5$ and $(2, 1)_8$, and one coupling mode, $(1, 2)_{13}$, so the corresponding mode amplitudes $A_5$, $A_8$, $A_{10}$, $A_{16}$, and $A_{13}$ can be obtained as the amplitudes of $a_{1,2,5}(t)$, $a_{1,1,8}(t)$, $a_{2,3,5}(t)$, $a_{2,1,8}(t)$, and $a_{1,2,13}(t)$, respectively. Figure 9 shows slow evolution of $A_5$, $A_8$, $A_{10}$, $A_{16}$ and $A_{13}$, where a temporary saturation of the fivefold mode is present. The phase portrait of $A_8$ versus $A_5$ in Fig. 10(a) clearly illustrates the growth and saturation of $(5, 2)$, the transitional process from $(5, 2)$ to $(8, 1)$, and the final saturation of $(8, 1)$. Harmonics $(m = 2)$ arise from the self-interaction of the primary modes, indicating $A_{2\nu}$ is of quadratic order in $A_\nu$ [see Figs. 10(b) and 10(c)]. The 13-fold mode emerges through the nonlinear interaction between two primary modes, exhibiting amplitude scaling $A_{13} \sim A_5 A_8$ [see Fig. 10(d)]. Formation of the $\nu$-fold mode involves nonlinear interactions among the primary modes, their harmonics, and the coupling mode. Therefore, for a complete dynamical description, additional terms such as $A_{10}^2 A_5$ $(\sim A_5^5)$, $A_{16}^2 A_5$ $(\sim A_8^4 A_5)$, and $A_{13}^2 A_5$ $(\sim A_8^2 A_5^3)$ must be included in the amplitude equation (4) for $A_5$, along with terms like $A_{16}^2 A_8$ $(\sim A_8^5)$, $A_{10}^2 A_8$ $(\sim A_5^4 A_8)$, and $A_{13}^2 A_8$ $(\sim A_5^2 A_8^3)$ in that for $A_8$. Furthermore, amplitude equations governing $A_{10}$, $A_{16}$, and $A_{13}$ should be incorporated in Eqs. (4), showing how they are driven by $A_5$ and $A_8$. The resulting system

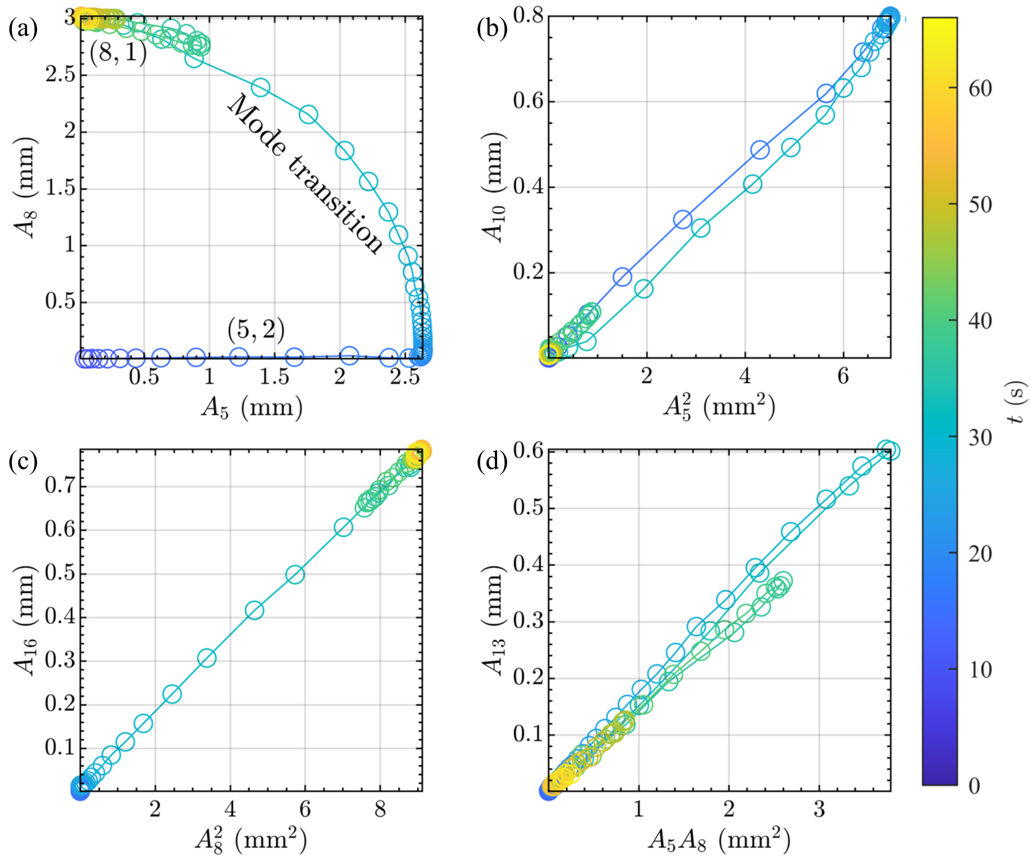


FIG. 10. Phase portraits among mode amplitudes: (a) $A_8$ vs $A_5$, (b) $A_{10}$ vs $A_5^2$, (c) $A_{16}$ vs $A_8^2$, and (d) $A_{13}$ vs $A_5A_8$. The same color bar of time $t$ is given for these subplots.

of amplitude equations becomes increasingly complicated, leading to difficulty in identifying the nonlinear coefficients. To thoroughly understand the nonlinear dynamics observed in double-mode systems, experimental measurement of mode amplitudes, with enhanced spatiotemporal resolution, should be further studied.

Note that the aforementioned transitional responses in the overlapping regime of two tongues are common. As shown in Fig. 11, another transitional response from a transient eightfold mode to a prevailing zerofold mode has been observed through careful force selection in the experiment

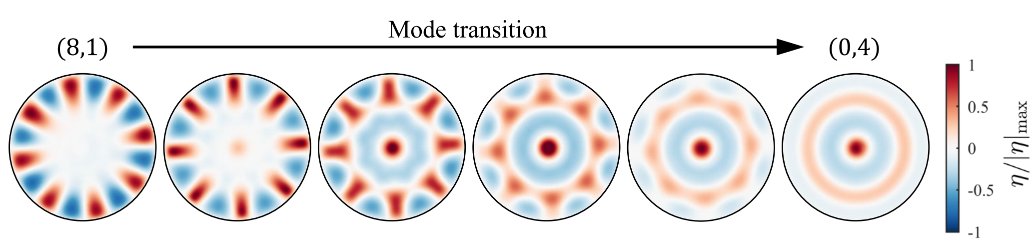


FIG. 11. Transitional response from (8, 1) to (0, 4) observed in the experiment for $\Gamma_0 = 0.18$ and $f = 16.95$ Hz. The color bar relates to the normalized surface elevation, $\eta/|\eta|_{\max}$, where $|\eta|_{\max}$ is the corresponding maximum of the absolute surface elevation.

for the simultaneous excitation of $(0, 4)$ and $(8, 1)$. Herein the tongue of $(0, 4)$ [not present in Fig. 4(a)] is adjacent to the left side of the $(8, 1)$ tongue, i.e., $f_0 < f_8$. In the double-mode system of $(8, 1)$ and $(0, 4)$, a single-point detection $\Psi_0 = \psi_0(\omega_0)$, obtained at the point $P_0$ $(r_p \approx 0)$ by LDV, can be employed to quickly estimate the gradual pattern development of the $(0, 4)$ mode because of the minor contribution of the eightfold mode to the surface deformation at the container's center. Analysis of surface reconstructions can also give similar transitional characteristics of mode amplitudes, as discussed in detail for the double-mode system of $(8, 1)$ and $(5, 2)$.

## V. CONCLUSIONS

Experimental observations have been made of mode transitions of Faraday waves in a brimful cylinder, with driving parameters selected near the overlap between two tongues. Particular attention is paid to two pure modes, $(5, 2)$ and $(8, 1)$, and their interactions. The behavior of Faraday waves in the double-mode system is experimentally measured using two optical methods that sensed the surface elevation: single-point motion measurement by LDV, and full 3D spatial reconstruction based on the FS-SS method. The experimental results exhibit a level of reproducibility that guarantees the synchronization between the single-point and full 3D surface evaluations obtained from separate sets of experiments. At two specially chosen points $P_\nu$ $(\nu = 5, 8)$ based on different contributions of two primary modes to the local surface elevation, the local oscillation amplitudes, $\Psi_\nu$ $(\nu = 5, 8)$, provide the time-dependent evolution of the two primary modes. In addition, the $(\nu, \zeta)$ mode is considered as the superposition of $\nu$-basis modes $(m, n)_\nu$ [30], and the fitting coefficients from surface reconstructions yield mode amplitudes $A_\nu$ for the primary components $(1, \zeta)_\nu$. The transformation factor from $\Psi_\nu$ to $A_\nu$ can be calculated using the experimental data obtained when the pattern formation reaches a steady state. When compared to full 3D identification of $A_\nu$, single-point measurement by LDV is quicker but less accurate especially when slight rotation of the pattern is present.

Based on our two optical methods, we report double-mode prevailing responses $(8, 1)^*$ (see Fig. 8), which offer an experimental realization of the numerical calculation for pattern-forming dynamics as presented by Meron and Procaccia [17]. Such transitional pattern formation from the rest state arises under combined conditions of a rapid initialization of the forcing acceleration from 0 to the prescribed $\Gamma_0$ and a fixed driving frequency $f$ slightly exceeding the bicritical $f_B$. The mode transition from a fivefold mode to an eightfold mode can be understood in the framework of two coupled amplitude equations (4), derived by Meron [18]. The mode suppression is characterized by the nonlinear interaction terms of opposite sign, $g_{8,5} > 0 > g_{5,8}$. Detailed analysis of $A_\nu(t)$ $(\nu = 5, 8)$ in the single-mode response yields $\alpha_\nu = \bar{\alpha}_\nu \epsilon_\nu$ and $\beta_5 > 0 > \beta_8$ in Eq. (5), in accordance with the derivation by Meron [18]. Since $\beta_5 > 0 > \beta_8$, the fivefold mode transitions from the rest state to the steady state via a supercritical bifurcation, while the eightfold mode undergoes a subcritical bifurcation. As for the double-mode response, pattern competition in the $\Gamma_C < \Gamma_0 < \Gamma_S$ regime has been widely studied, and herein our sole focus is on the prevailing mode transition in the regime of $\Gamma_0 > \Gamma_S$. The time-varying mode amplitudes determined from surface fits imply that harmonics $(\nu = 10, 16)$ and the competing mode $(\nu = 13)$ should be included as fifth-order terms in Eqs. (4). Additionally, the equations for $A_{10}$, $A_{16}$, and $A_{13}$ should also be incorporated into the system of amplitude equations, complicating the identification of the associated nonlinear coefficients.

Transitional response of double-mode Faraday waves is a common nonlinear phenomenon in the vicinity of the corresponding bicritical point on the higher frequency side, such as encountered in the mode transition from $(8, 1)$ to $(0, 4)$ (see Fig. 11). It is feasible to extend our experimental techniques and phenomenological analysis to multimode systems that encompass the overlapping region of three or more pure modes. For instance, a potential three-mode system could be identified in the higher acceleration amplitude regime $(\Gamma_0 > 0.2)$, where the $(0, 4)$ region extends into the overlap between the $(5, 2)$ and $(8, 1)$ tongues. In such a three-mode system, the local amplitude detected via LDV at three selected points $P_\nu$ $(\nu = 0, 5, 8)$ can be employed to quickly characterize the pattern-forming behaviors of the three corresponding primary modes. Mode amplitudes $A_\nu$ $(\nu =$

0, 5, 8) can also be calculated from the best fit of surface constructions. Additionally, Eqs. (4) can be readily updated to three coupled amplitudes of $A_\nu$ ($\nu = 0, 5, 8$) to describe transitional responses in a three-mode system; this will be our future focus.

## ACKNOWLEDGMENTS

The authors are indebted to Prof. Alistair G. L. Borthwick (Universities of Edinburgh and Plymouth, and St Edmund Hall, Oxford) for his beneficial discussions and valuable suggestions. The authors also acknowledge support from the National Natural Science Foundation of China (Grants No. 52371287 and No. 51979162) and the Oceanic Interdisciplinary Program of Shanghai Jiao Tong University (Grant No. SL2021MS019).

## DATA AVAILABILITY

The data supporting this study's findings are available within the article.

[1] M. Faraday, XVII. On a peculiar class of acoustical figures; and on certain forms assumed by groups of particles upon vibrating elastic surfaces, Philos. Trans. R. Soc. London **121**, 299 (1831).

[2] L. Matthiessen, Akustische Versuche, die kleinsten Transversalwellen der Flüssigkeiten betreffend, Ann. Phys. **210**, 107 (1868).

[3] T. B. Benjamin and F. J. Ursell, The stability of the plane free surface of a liquid in vertical periodic motion, Proc. R. Soc. London A **225**, 505 (1954).

[4] K. Kumar and L. S. Tuckerman, Parametric instability of the interface between two fluids, J. Fluid Mech. **279**, 49 (1994).

[5] J. Bechhoefer, V. Ego, S. Manneville, and B. Johnson, An experimental study of the onset of parametrically pumped surface waves in viscous fluids, J. Fluid Mech. **288**, 325 (1995).

[6] O. Lioubashevski, J. Fineberg, and L. S. Tuckerman, Scaling of the transition to parametrically driven surface waves in highly dissipative systems, Phys. Rev. E **55**, R3832 (1997).

[7] K. Kumar, Linear theory of Faraday instability in viscous liquids, Proc. R. Soc. London A **452**, 1113 (1996).

[8] H. W. Müller, H. Wittmer, C. Wagner, J. Albers, and K. Knorr, Analytic stability theory for Faraday waves and the observation of the harmonic surface response, Phys. Rev. Lett. **78**, 2357 (1997).

[9] C. Wagner, H. W. Müller, and K. Knorr, Pattern formation at the bicritical point of the Faraday instability, Phys. Rev. E **68**, 066204 (2003).

[10] W. Batson, F. Zoueshtiagh, and R. Narayanan, The Faraday threshold in small cylinders and the sidewall non-ideality, J. Fluid Mech. **729**, 496 (2013).

[11] A. Briard, B.-J. Gréa, and L. Gostiaux, Harmonic to subharmonic transition of the Faraday instability in miscible fluids, Phys. Rev. Fluids **4**, 044502 (2019).

[12] S. Ciliberto and J. P. Gollub, Pattern competition leads to chaos, Phys. Rev. Lett. **52**, 922 (1984).

[13] S. Ciliberto and J. Gollub, Chaotic mode competition in parametrically forced surface waves, J. Fluid Mech. **158**, 381 (1985).

[14] S. Ciliberto and J. Gollub, Phenomenological model of chaotic mode competition in surface waves, Il Nuovo Cimento D **6**, 309 (1985).

[15] F. Simonelli and J. P. Gollub, Surface wave mode interactions: Effects of symmetry and degeneracy, J. Fluid Mech. **199**, 471 (1989).

[16] E. Meron and I. Procaccia, Low-dimensional chaos in surface waves: Theoretical analysis of an experiment, Phys. Rev. A **34**, 3221 (1986).

[17] E. Meron and I. Procaccia, Theory of chaos in surface waves: The reduction from hydrodynamics to few-dimensional dynamics, Phys. Rev. Lett. **56**, 1323 (1986).

[18] E. Meron, Parametric excitation of multimode dissipative systems, Phys. Rev. A **35**, 4892 (1987).
[19] M. Umeki and T. Kambe, Nonlinear dynamics and chaos in parametrically excited surface waves, J. Phys. Soc. Jpn. **58**, 140 (1989).
[20] B. Christiansen, P. Alstrøm, and M. T. Levinsen, Ordered capillary-wave states: Quasicrystals, hexagons, and radial waves, Phys. Rev. Lett. **68**, 2157 (1992).
[21] C. Wagner, H. W. Müller, and K. Knorr, Faraday waves on a viscoelastic liquid, Phys. Rev. Lett. **83**, 308 (1999).
[22] P. Chen and J. Viñals, Amplitude equation and pattern selection in Faraday waves, Phys. Rev. E **60**, 559 (1999).
[23] D. K. Raja, E. J. Hopfinger, and S. P. Das, Conditions of inertial-viscous transition and related jetting in large cavity collapse, Phys. Rev. Fluids **5**, 124002 (2020).
[24] M. Kharbedia, N. Caselli, D. Herráez-Aguilar, H. López-Menéndez, E. Enciso, J. A. Santiago, and F. Monroy, Moulding hydrodynamic 2D-crystals upon parametric Faraday waves in shear-functionalized water surfaces, Nat. Commun. **12**, 1130 (2021).
[25] R. Kidambi, Meniscus effects on the frequency and damping of capillary-gravity waves in a brimful circular cylinder, Wave Motion **46**, 144 (2009).
[26] P. Wilson, X. Shao, J. R. Saylor, and J. B. Bostwick, Role of edge effects and fluid depth in azimuthal Faraday waves, Phys. Rev. Fluids **7**, 014803 (2022).
[27] A. Bongarzone, F. Viola, S. Camarri, and F. Gallaire, Subharmonic parametric instability in nearly brimful circular cylinders: A weakly nonlinear analysis, J. Fluid Mech. **947**, A24 (2022).
[28] X. Shao, C. T. Gabbard, J. B. Bostwick, and J. R. Saylor, On the role of meniscus geometry in capillary wave generation, Exp. Fluids **62**, 59 (2021).
[29] X. Shao, P. Wilson, J. R. Saylor, and J. B. Bostwick, Surface wave pattern formation in a cylindrical container, J. Fluid Mech. **915**, A19 (2021).
[30] S. Zhang, A. G. L. Borthwick, and Z. Lin, Pattern evolution and modal decomposition of Faraday waves in a brimful cylinder, J. Fluid Mech. **974**, A56 (2023).
[31] F. Simonelli and J. P. Gollub, Stability boundaries and phase-space measurement for spatially extended dynamical systems, Rev. Sci. Instrum. **59**, 280 (1988).
[32] Z. Feng and P. R. Sethna, Symmetry-breaking bifurcations in resonant surface waves, J. Fluid Mech. **199**, 495 (1989).
[33] F. Moisy, M. Rabaud, and K. Salsac, A synthetic Schlieren method for the measurement of the topography of a liquid interface, Exp. Fluids **46**, 1021 (2009).
[34] F. Moisy, G.-J. Michon, M. Rabaud, and E. Sultan, Cross-waves induced by the vertical oscillation of a fully immersed vertical plate, Phys. Fluids **24**, 022110 (2012).
[35] A. P. Damiano, P.-T. Brun, D. M. Harris, C. A. Galeano-Rios, and J. W. Bush, Surface topography measurements of the bouncing droplet experiment, Exp. Fluids **57**, 163 (2016).
[36] A. P. Abella and M. N. Soriano, Detection and visualization of water surface three-wave resonance via a synthetic Schlieren method, Phys. Scr. **94**, 034006 (2019).
[37] S. Dehe, M. Hartmann, A. Bandopadhyay, and S. Hardt, The spatial structure of electrostatically forced Faraday waves, J. Fluid Mech. **939**, A6 (2022).
[38] D. M. Henderson and J. W. Miles, Faraday waves in 2:1 internal resonance, J. Fluid Mech. **222**, 449 (1991).
[39] F. Haudin, A. Cazaubiel, L. Deike, T. Jamin, E. Falcon, and M. Berhanu, Experimental study of three-wave interactions among capillary-gravity surface waves, Phys. Rev. E **93**, 043110 (2016).
[40] J. Yang and K. Bhattacharya, Augmented Lagrangian digital image correlation, Exp. Mech. **59**, 187 (2019).
[41] S. P. Das and E. J. Hopfinger, Parametrically forced gravity waves in a circular cylinder and finite-time singularity, J. Fluid Mech. **599**, 205 (2008).
[42] R. D. Henderson and D. Barkley, Secondary instability in the wake of a circular cylinder, Phys. Fluids **8**, 1683 (1996).
[43] See Supplemental Material at http://link.aps.org/supplemental/10.1103/PhysRevFluids.10.034003 for the movie that shows the transitional pattern formation.